Depletion-Induced Intermediate-Range Order Modulates Nanoscale Protein Diffusion in Polymeric Crowder Solutions

Michelle Dargasz [1*], Nimmi Das Anthuparambil[1], Sebastian Retzbach[2], Anita Girelli[3], Sonja Timmermann[1], Johannes Möller[4], Wonhyuk Jo[4], Aliaksandr Lenonau[1,4], Agha Mohammad Raza[1], Maddalena Bin[3], Jaqueline Savelkouls[5], Iason Andronis[3], Frederik Unger[1], Felix Brausse[4], Jörg Hallmann[4], Ulrike Boesenberg[4], Jan-Etienne Pudell[4], Angel Rodriguez-Fernandez[4], James Wrigley[4], Roman Shayduk[4], Mohamed Youssef[4], Alexey Zozulya[4], Anders Madsen[4], Felix Lehmkühler[6,7], Fivos Perakis[3], Fajun Zhang[2], Frank Schreiber[2], Michael Paulus[5], Christian Gutt [1†]

[1]Department Physik, Universität Siegen, Walter-Flex-Strasse 3, 57072 Siegen, Germany
[2]Institut für Angewandte Physik, Universität Tübingen, Auf der Morgenstelle 10, 72076 Tübingen, Germany
[3]Department of Physics, AlbaNova University Center, Stockholm University, 10691 Stockholm, Sweden
[4]European X-Ray Free-Electron Laser Facility, Holzkoppel 4,22869 Schenefeld, Germany
[5]Fakultät Physik/DELTA, TU Dortmund, 44221 Dortmund, Germany
[6]The Hamburg Centre for Ultrafast Imaging, Luruper Chaussee 149, 22761 Hamburg, Germany
[7]Deutsches Elektronen-Synchrotron DESY, Notkestr. 85, 22607 Hamburg, Germany

[*]Corresponding author. Email: michelle.dargasz@uni-siegen.de
[†]Corresponding author. Email: christian.gutt@uni-siegen.de

Classification: Physical Science, Biophysics and Computational Biology

Keywords:
macromolecular crowding; diffusion;
X-ray photon correlation spectroscopy; Free-Electron Laser

Abstract

Macromolecular crowding plays a crucial role in modulating protein dynamics in cellular and in vitro environments. While traditionally attributed to excluded volume effects, many commonly used polymeric crowders — such as dextran and Ficoll - induce additional entropic forces, including depletion interactions, that influence protein behavior on nanometer length scales. Using Megahertz X-ray photon correlation spectroscopy (MHz-XPCS) at the European XFEL, we investigated the nanoscale dynamics of ferritin in solutions of sucrose, dextran, and Ficoll. Our measurements reveal that polysaccharide crowders induce short-range attractions and intermediate-range order (IRO) beyond the polymer overlap concentration c^*, driven by depletion effects that vary with crowder type and molecular weight. These IRO features fluctuate on microsecond to millisecond timescales enhancing protein assembly. By normalizing concentration to c^*, we observe a scaling trend with a crossover near $2c^*$, marking a shift from depletion-enhanced mobility to viscosity-dominated slowing. Our results challenge the assumption that polymeric crowders act as inert background agents, demonstrating instead that their structural properties and concentration regimes critically influence protein dynamics. This study highlights the need to incorporate polymer physics and depletion theory into models of crowded environments, where even standard crowders exhibit system-specific, nontrivial effects.

Significance statement

Understanding how proteins move and interact in crowded environments is essential for unraveling the physical basis of cellular processes. While polymer-based crowders like dextran and Ficoll are widely used to mimic intracellular crowding, they are often treated as inert background agents. Our study challenges this assumption by showing that these crowders actively modulate protein dynamics through depletion interactions and the formation of transient nanoscale structures. Using MHz-XPCS at the European XFEL, we uncover how polymer concentration and molecular weight reshape protein diffusion and organization. These findings highlight the need to move beyond simplistic crowding models and incorporate concepts from polymer physics to more accurately describe biomolecular behavior in complex environments.

Introduction

Macromolecular crowding is a defining feature of the cellular environment [1], where high concentrations of macromolecules significantly influence protein dynamics [2–4], a key factor in processes such as molecular transport, signal transduction, and enzymatic activity [5–7]. Traditionally, crowding effects have been attributed to excluded volume interactions, especially when crowders are modeled as hard spheres [1] [8–12]. However, many commonly used "inert" crowders — such as dextran, Ficoll, or polyethylene glycol (PEG) — are flexible polymers whose influence extends beyond steric hindrance [13–15]. In these systems, entropic interactions, polymer overlap and network structures with their associated correlation lengths become key descriptors [16–19].

A well-known outcome of such entropic interactions is depletion attraction, where non-adsor-

bing polymers generate effective forces that promote protein association [20–22]. These interactions can lead to reversible aggregation, conformational shifts, and liquid–liquid phase separation (LLPS) into protein-rich and protein-poor phases, a mechanism increasingly linked to the formation of membraneless organelles [23–30]. However, even before bulk phase separation occurs, proteins can form clusters and intermediate-range order (IRO) on nanometer length scales, governed by a balance of short-range attractions and long-range repulsions [31, 32].

Such crowder driven structural organization also profoundly impacts protein dynamics [33]. In polymeric solutions, proteins frequently exhibit anomalous diffusion, characterized by nonlinear mean squared displacements that are well-described by models such as fractional Brownian motion (fBM), capturing the viscoelastic constraints imposed by the surrounding polymer network [34–38]. Crowding also modulates biochemical reactions, either by hindering diffusion or by enhancing complex formation through entropic and enthalpic attractive interactions [39–45]. These effects occur on the nanoscale, making it essential to understand the local structure, single-particle diffusion, and collective dynamics at nanometer length scales. In terms of timescales, these processes unfold over the microsecond to millisecond range, a regime ideally suited for investigation using megahertz X-ray photon correlation spectroscopy (MHz-XPCS).

To probe nanoscale crowding effects, we employed MHz-XPCS at the European XFEL to measure ferritin dynamics in solutions of sucrose, dextran, and Ficoll. Increasing crowder concentration significantly alters collective diffusion, indicating transient intermediate-range order (IRO) driven by depletion-enhanced attractions. This structural order decays on microsecond to millisecond timescales and coincides with reduced hydrodynamic interactions. Our measurements enable quantification of depletion strengths, even for nominally inert crowders, and allow estimation of protein cluster lifetimes. Ferritin self-diffusion exhibits a non-monotonic dependence on crowder concentration, linked to the polymer overlap concentration and depletion layer thickness. These deviations from expected scaling — similar to those observed for nanoparticles in PEG solutions [46] — underscore the importance of nanoscale effects that remain invisible to bulk measurements.

These insights point towards the profound influence of macromolecular crowding on protein dynamics through modifications to interaction potentials and local structure. In this context, the long-standing assumption that synthetic polymer crowders act as inert, non-interacting background agents needs to be re-evaluated. Crowders such as dextran and Ficoll, often considered passive, may in fact contribute to emergent structure formation and alter local interaction landscapes.

Our findings motivate a more detailed view of macromolecular crowding using polymers — one that integrates depletion interactions, polymer network structure, and transient nanoscale order as key contributors to protein mobility and phase behavior in complex environments.

Results

XPCS as a tool to probe the nanoscale impact of crowding on protein dynamics. We investigate the effects of standard crowders on protein dynamics via MHz-XPCS experiments at the Materials Imaging and Dynamics (MID) instrument of European XFEL. The technique enables direct measurement of collective and self-diffusion at nanoscopic length scales and mi-

crosecond timescales, even in highly concentrated solutions. Additionally, XPCS provides also access to the hydrodynamic function, aiding in the study of long-range many-body interactions mediated by the solvent. These capabilities make MHz-XPCS a powerful tool for investigating molecular crowding effects. Its application for measuring protein dynamics has been successfully demonstrated by Reiser et al. [47], Girelli et al. [48] and DasAnthuparambil et al. .

Modeling a crowded environment utilizing standard crowding agents. In this study, we used the protein ferritin, dissolved in various macromolecular crowders. Ferritin is a spherical protein complex composed of 24 subunits that assemble into a hollow shell capable of storing up to 4,500 Fe(III) atoms [49, 50], thus fulfilling its primary function in iron storage [51]. Due to its high monodispersity and stability over a broad range of pH and temperature conditions, ferritin is also widely used in vaccine development [52] and drug delivery applications [53, 54]. These attributes, combined with the strong X-ray scattering contrast provided by its iron-rich core, make ferritin an ideal globular model protein for X-ray scattering studies under concentrated and crowded conditions. Several standard crowding agents of varying molecular sizes were used, including the nanocrowder sucrose (M_w= 342.3 g/mol) and the polysaccharides Ficoll400 (M_w= 400 kg/mol) and dextran with three different molecular weights (M_w= 40, 100, 500 kg/mol).

Accessing protein dynamics by extracting intensity autocorrelation functions. Samples were loaded into quartz-glass capillaries, sealed with epoxy glue, and examined using MHz-XPCS at the Materials Imaging and Dynamics (MID) instrument [55]. The experimental setup is illustrated in Fig. 1. We report results from two experimental campaigns utilizing photon energies of 9 and 10 keV and beam sizes of 14.5 and 13 µm, respectively. X-ray pulse trains containing 200 respective 310 pulses with a spacing of 440 and 222 ns interacted with the sample, and pulse-resolved scattering patterns were recorded by the Adaptive Gain Integrating Pixel Detector (AGIPD), positioned 7.15 m and 7.68 m from the sample. This configuration provided access to wavevectors in the range $q = 0.1 - 0.6$ nm^{-1} as well as $0.075 - 0.6$ nm^{-1} and enabled measurements on time scales from 0.44 to 88 µs and 0.22 to 69 µs.

To reduce radiation damage and beam-induced heating, the X-ray intensity was strongly attenuated by an absorber transmission of 0.02%, and the sample volume was refreshed for each pulse train. As a result, the X-ray dose and dose rate remained below established damage thresholds as demonstrated in [48][Nimmi]. Statistically robust results were obtained by averaging scattering patterns and autocorrelation functions from thousands of distinct positions along each capillary. In addition to the MHz-XPCS experiments, complementary small-angle X-ray scattering (SAXS) measurements were performed at the DELTA synchrotron facility at TU Dortmund [56].

The collected scattering signal is dominated by the contribution of ferritin, whose scattering intensity is approximately two orders of magnitude higher than that of the corresponding pure crowder solutions (*SI Appendix*, Fig.S1). Protein dynamics were analyzed by calculating intensity autocorrelation functions, $g_2(q,t)$, from the temporal intensity fluctuations of the speckle patterns recorded within a single X-ray pulse train. Fig.1B presents an example of the resulting q-dependent $g_2(q,t)$-functions, where q refers to the momentum transfer as $q = 4\pi/\lambda \sin(2\theta/2)$ with 2θ denoting the scattering angle. The $g_2(q,t)$-functions were collected at room temperature using a constant ferritin concentration of 55 mg/ml and varying crowder concentrations of 10

up to 40 %w/w. The solid lines represent a stretched exponential fit, described by [57]:

$$g_2(q,t) = 1 + \beta(q)\exp[-2\,(\Gamma(q)\,t)^{\alpha}] \tag{1}$$

where $\beta(q)$ denotes the q-dependent speckle contrast, which was modeled as described in [58,59]. $\Gamma(q)$ represents the q-dependent relaxation rate, and α corresponds to the Kohlrausch-Williams-Watts (KWW) exponent. All correlation functions were well described using a Kohlrausch-Williams-Watts (KWW) exponent of 0.9. This value reflects slightly sub-diffusive behavior, consistent with previous observations for the diffusion of nanoparticles, proteins, and fluorescent tracers in solutions containing soft polymers [60–62]. More details on extracting the $g_2(q,t)$-function can be found in the Methods section.

Fig.1C shows the $g_2(t)$-functions of ferritin in dextran40 solutions at varying concentrations, revealing slower dynamics with increasing crowder concentration due to reduced macromolecular mobility caused by the increasing excluded volume for ferritin. Fig.1D compares ferritin dynamics in solutions with different crowders at 20 %w/w. Ferritin in sucrose solutions exhibits significantly faster dynamics than in polysaccharide-based solutions. This difference is attributed to overlapping polymer chains in polysaccharides which increase the solution viscosity, further restricting protein mobility.

Collective protein dynamics in sucrose solution exhibits repulsive behavior. In crowded solutions with high particle concentrations, protein dynamics are influenced by both direct protein-protein interactions and indirect hydrodynamic interactions mediated by the solvent [64]. These interactions lead to a wavevector-dependent collective diffusion coefficient, $D(q)$, that is related to the static structure factor $S(q)$, the hydrodynamic function $H(q)$, and the diffusion coefficient at infinite dilution D_0 as [65]

$$D(q) = D_0 \cdot \frac{H(q)}{S(q)}. \tag{2}$$

The structure factor, $S(q)$, which reflects static interparticle correlations, is commonly determined in SAXS experiments by dividing the scattering intensity of a concentrated solution by that of a dilute one, thereby isolating interparticle effects from the single-particle form factor. However, in binary solutions where the two components exhibit concentration dependent scattering signatures due to changes in polymer correlation lengths and electron density contrast, a direct extraction of $S(q)$ corresponding solely to ferritin–ferritin interactions becomes challenging. In such systems, the experimentally accessible diffusion coefficient $D(q)$ provides an alternative means of investigation, as it is inversely related to $S(q)$ following Eq. 2 [66]. The diffusion coefficient $D(q)$ is extracted from exponential fits to the intensity autocorrelation functions, g_2, using the relation $D(q) = \Gamma(q)/q^2$. As shown in Fig. 2A, the $D(q)$ of ferritin in sucrose solution decreases with increasing q until reaching a minimum at typical values of the maximum of structure factors characteristic of repulsive behavior. This observation is consistent with recent measurements of the collective ferritin diffusion in aqueous solutions [48].

Depletion-induced IRO in polysaccharide solutions affects collective protein dynamics.

The collective dynamics of ferritin in polysaccharide solutions are presented in Fig. 2B–E.

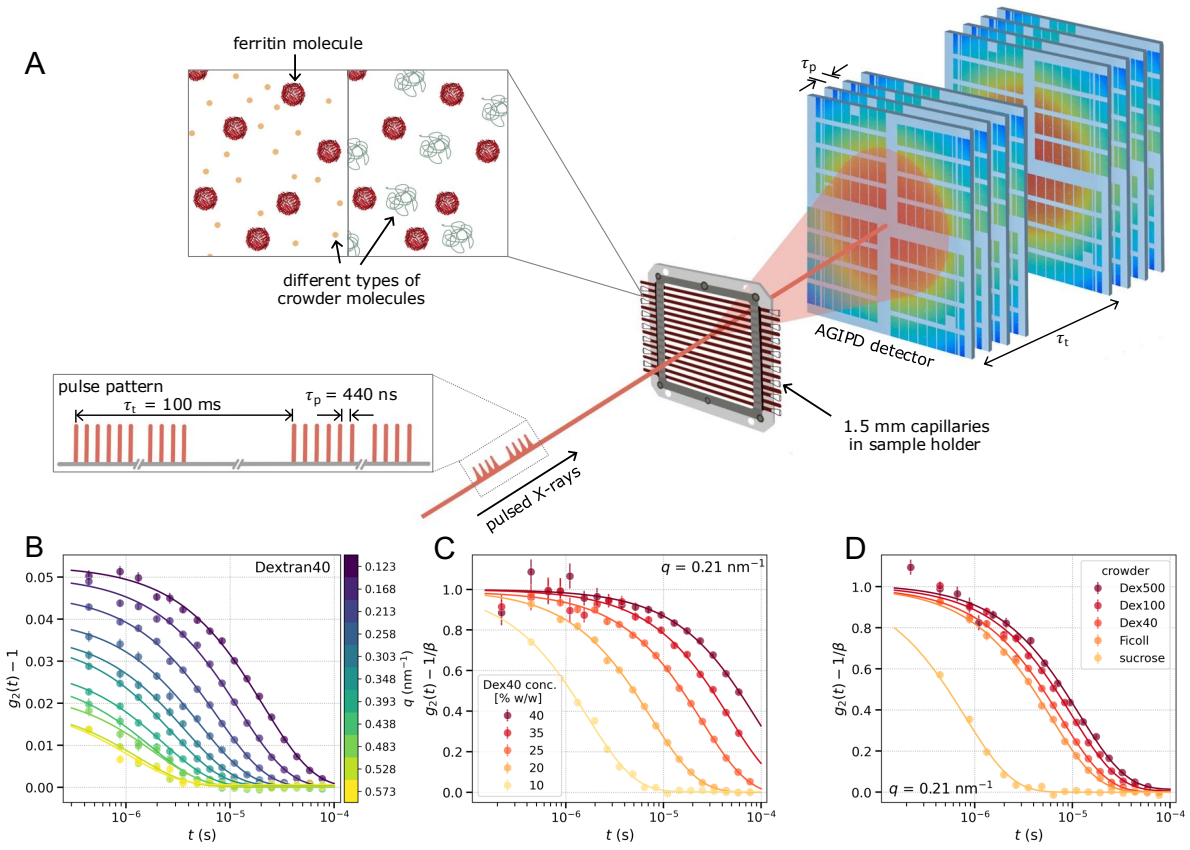

Fig. 1. MHz-XPCS data collection at MID instrument of European XFEL. (A) Schematic representation of the experimental setup. Ferritin solutions with a fixed ferritin concentration of 55 mg/ml and varying types and concentrations of crowder molecules are filled in quartz capillaries. Coherent and pulsed X-rays illuminate the protein solution, generating speckle patterns recorded by the adaptive gain integrated pixel detector (AGIPD). A new train is delivered every 100 ms, with pulse spacings between 440 ns and 220 ns. The intensity fluctuations within a train are analyzed to extract dynamic information by calculating intensity autocorrelation functions ($g_2(t)$). To ensure sufficient scattering contrast, $g_2(t)$-functions are averaged over approximately 12.000 trains. (B) q-dependent $g_2(t)$-functions for ferritin in a 25 %w/w dextran40 solution. (C) $g_2(t)$-functions at a fixed q-value of 0.21 nm^{-1} for various dextran40 concentrations ranging from 10 to 40 %w/w. (D) $g_2(t)$-functions at the same q-value for different crowder molecules: dextran500, dextran100, dextran40, Ficoll400, and sucrose. Solid lines represent exponential fits based on Eq. 1. The calculation of the errorbars is described in Methods. Schematic of ferritin molecules was taken from PDB ID:2w0o [63].

Similar to ferritin in sucrose the pronounced minimum in the q-range of 0.54 – 0.57 nm^{-1} corresponds to the typical ferritin monomer-monomer peak position of the static structure factor. However, in contrast to sucrose solutions, increasing the concentration of polymeric crowders leads to the emergence of a second minimum at lower q-values. This results in a deviation from the typical monotonic decrease in $D(q)$ characteristic of repulsive systems (dotted line in Fig. 2E). Such behavior indicates the presence of short-range attractive interactions superimposed on long-range repulsion, consistent with the development of intermediate-range order (IRO).

IRO is characterized by spatial correlations over intermediate length scales — typically 2–3 protein diameters — arising from competing interactions rather than stable aggregation or clustering [32, 67]. In such weakly correlated systems, the size distribution is dominated by monomeric ferritin, with only a minor fraction forming transient complexes. These complexes are defined by short-lived associations, where proteins dynamically exchange between monomeric

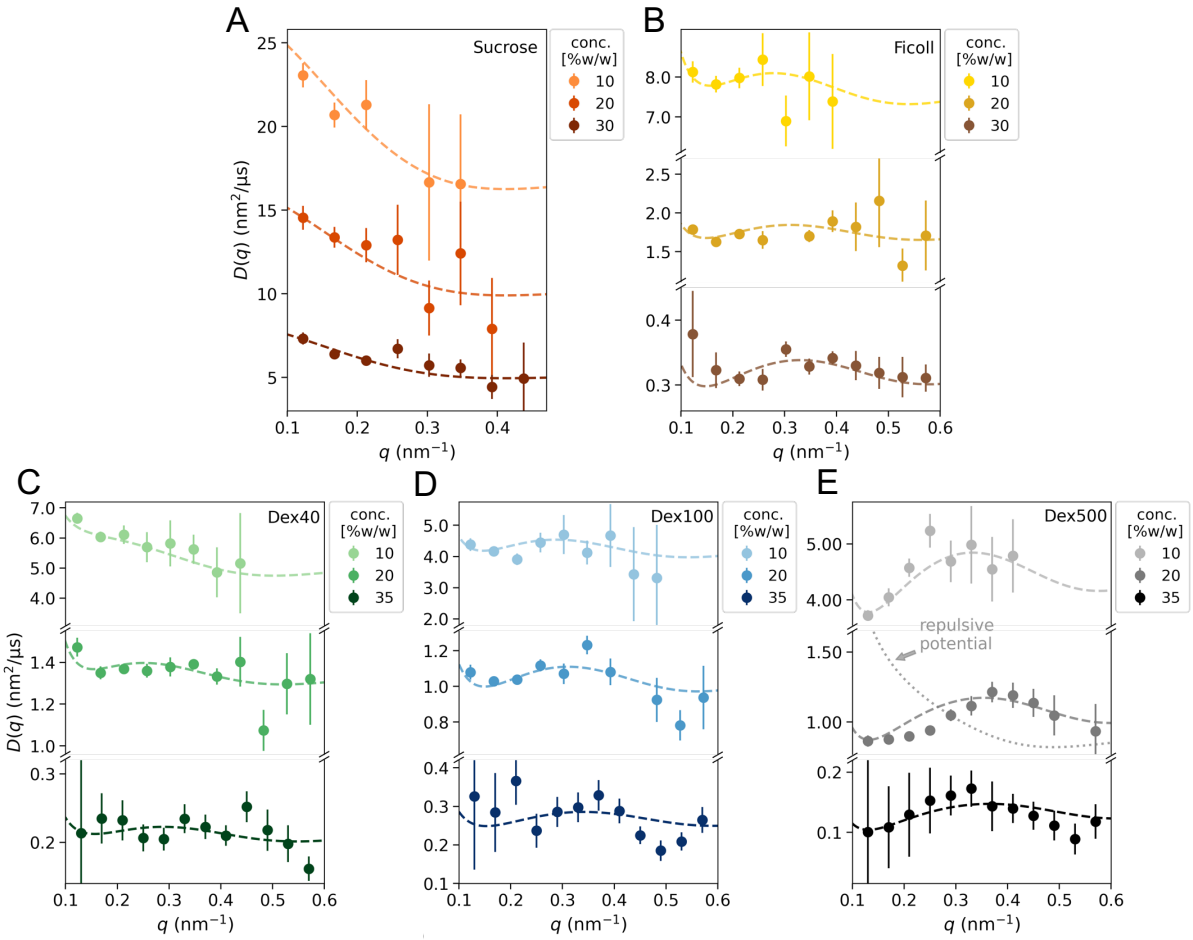

Fig. 2. Extracted q-dependent collective diffusion coefficients $D(q) = \Gamma(q)/q^2$ of ferritin in crowded solutions. $D(q)$ of ferritin in solution with 10, 20 and 30 %w/w (A) sucrose and (B) Ficoll400 as well as with 10, 20 and 35 %w/w (C) dextran40, (D) dextran100 and (E) dextran500. The dashed lines represent the calculated $D(q)$ based on (A) a single-Yukawa and (B) - (E) a two-Yukawa potential as further described in Methods. Errorbars are calculated from g_2-fits using least-squares minimization.

and associated states [32]. As a result, the IRO remains dynamic, with structural fluctuations occurring on the microsecond timescale, as revealed by our XPCS measurements.

Nevertheless, this intermediate range structural organization reduces protein mobility at the corresponding length scale as evidenced by the comparison with a repulsive interaction only (Fig. 2E). IRO has been observed in concentrated lysozyme [68, 69] and monoclonal antibody (mAb) solutions [70], where enhanced attractive interactions arise from increased protein concentrations or specific inter-protein interactions.

In systems containing polymer-like crowders, depletion interactions provide a well-established mechanism for short-range attraction. As polymers lose configurational entropy near colloidal surfaces, polymer-depleted regions form around the particles [20–22]. When these regions overlap, the excluded volume inaccessible to the polymers is reduced, increasing the system's entropy and inducing an effective attractive force between colloids that promotes IRO formation. Our results clearly demonstrate that such depletion-induced interactions can significantly influence collective protein dynamics, highlighting that crowding effects extend beyond simple excluded volume constraints.

Occurrence of IRO is connected to overlap concentration of polysaccharides. The

transition from a simple decline in $D(q)$ to the emergence of a second minimum occurs when the polymer overlap concentration c^* is exceeded, as observed for dextran40 (c^*= 12.75 %w/w, Fig. 2C). This value was determined via macroscopic viscosity measurements (*SI Appendix*, Table S1). The overlap concentration c^* marks the onset of the semi-dilute regime, in which the correlation length ξ replaces the polymer's radius of gyration as the key structural length scale. ξ defines the distance beyond which polymer–polymer interactions are screened by neighboring chains, and thus governs the depletion layer thickness and the strength of the depletion-induced attraction. As polymer concentration increases, the correlation length decreases (see Fig. 4D), suggesting that an optimal size ratio for depletion interaction is achieved only when $c_{poly} > c^*$. This highlights the critical role of concentration-dependent polymer structure in modulating nanoscale collective protein dynamics.

Extracting structural and hydrodynamic information from protein dynamics. The dashed lines in Fig.2 represent modeled $D(q)$ curves based on Eq. 2. As direct direct experimental access to $S(q)$ is not easily feasible in these binary mixtures, $S(q)$ was instead computed from the underlying particle-particle interaction potentials, as described in the Methods section. To capture both the short-range attraction and long-range repulsion present in polysaccharide-containing solutions, a two-Yukawa potential was employed - a model commonly used to describe systems exhibiting IRO [69]. The reduced potential has the form [71]:

$$\frac{U(x)}{k_b\,T} = \begin{cases} -K_1\frac{e^{-Z_1(r-1)}}{r} - K_2\frac{e^{-Z_2(r-1)}}{r} & \text{for } r > 1 \\ \infty & \text{for } 0 < r < 1 \end{cases} \tag{3}$$

where Z_i= $1/scl_i$ denotes the inverse screening length, K_i the potential strength in $k_b\,T$ and r is scaled to yield a hardcore diameter of 1. For sucrose solutions, in which repulsive interactions dominate, a single-Yukawa potential was used by setting $K_1 = 0$ in Eq. 3 and the hydrodynamic function was calculated based on the $\delta\gamma$ expansion of Benakker and Mazur [72,73] (see Methods for details). By optimizing the potential parameters and the free diffusion coefficient D_0, an empirical model for $D(q)$ was obtained. The corresponding interaction potentials are shown in *SI Appendix*, Fig.S2, and the fitted parameters are listed in Table S2.

Despite the empirical nature of the models and the simplicity of the assumed potentials, the calculated $D(q)$ shows remarkable agreement with the experimental data. The modeled structure factor $S(q)$ for ferritin in dextran100 solutions (Fig.3A) exhibits a pronounced low-q peak, characteristic of IRO. Although a proper extraction of the pure ferritin–ferritin $S(q)$ from SAXS is not possible (as discussed earlier), an effective structure factor—including cross-correlations—can be obtained by dividing the background-subtracted SAXS intensity of a concentrated ferritin–crowder solution by that of a dilute solution with the same crowder concentration (Fig.3C). The observed increase in scattering intensity at low q in the experimental data further supports the presence of IRO.

Depletion attraction scales with crowder concentration and molecular weight. The concentration-dependent structure factor $S(q)$ (Fig.3A) and hydrodynamic function $H(q)$ (Fig.3B) for ferritin in dextran100 solutions both reveal that the IRO becomes increasingly pronounced with rising concentration. Since $H(q) = 1$ corresponds to the absence of hydrodynamic interactions, the observed increase in $H(q)$ at intermediate q-values suggests a weakening of

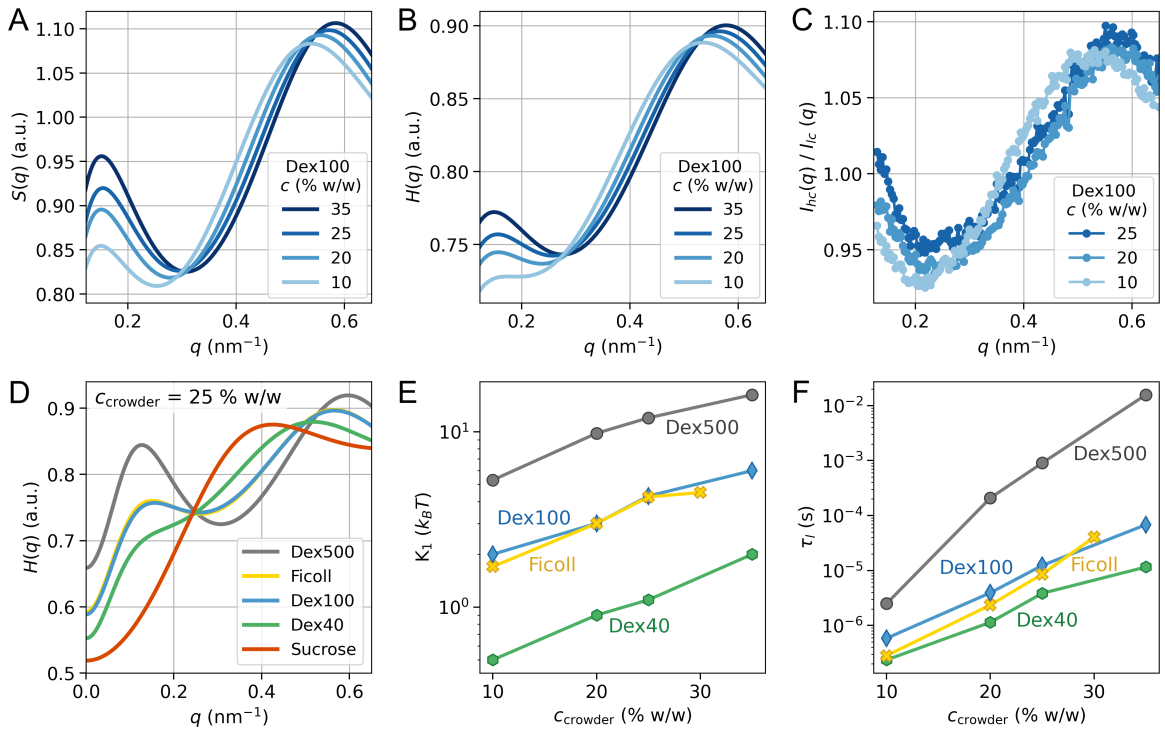

Fig. 3. Effects of concentration and molecular weight on the structure formation due to IRO. Results of the modeled (A) $S(q)$ and (B) $H(q)$ based on a two-Yukawa potential for ferritin in solution with 10, 20, 25 and 35 %w/w dextran100. (C) Experimentally measured small angle X-ray scattering (SAXS) intensity of 55 mg/ml ferritin in solution with 10, 20 and 25 %w/w dextran divided by SAXS intensity of 5 mg/ml ferritin in solution with the same dextran concentration. (D) $H(q)$ for all crowders at a concentration of 25 %w/w, illustrating the pronounced effect of increasing attractive interactions on sedimentation velocity, in contrast to the predominantly repulsive sucrose solution. (E) Attractive potential strength parameter K_1, and (F) lifetime of complexes formed via IRO, as a function of crowder concentration in polysaccharide systems. Both figures reveal a strong dependence on molecular weight, with higher molecular weight dextrans exhibiting significantly enhanced attractive interactions and correspondingly longer complex lifetimes.

hydrodynamic hindrance associated with the formation of IRO. This close connection between $S(q)$ and $H(q)$ is well known and reflects the reduced hydrodynamic drag in systems where correlated particle motion leads to more coherent flow patterns and less mutual interference.

The hydrodynamic function also provides insight into sedimentation coefficient, as $H(q \to 0) = K = V_{sed}/V_0$ with V_{sed} denoting the mean sedimentation velocity in a concentrated dispersion and V_0 the single-particle sedimentation velocity [74]. Sedimentation is a key contributor to mass transport and thus plays a critical role in the efficient distribution of biomolecules within cells [75,76] as well as in modulating phase separation. Figure 3D shows $H(q)$ for ferritin in 25 %w/w solutions of various crowders. The sedimentation coefficient K is low in solutions dominated by repulsive interactions, such as sucrose, and increases in the presence of polysaccharides like dextran500, which induce short-range attractive interactions. This enhanced sedimentation coefficient in systems with short-range attraction suggests that macromolecular crowding by polysaccharides can promote more efficient transport processes and facilitate phase separation.

The observed dependence of structure and dynamics on both molecular weight and crowder concentration is correlated with an enhanced depletion attraction, as evidenced by the growing attractive potential strength parameter K_1, shown in Fig 3E, and the increasing interaction

potential depth (*SI Appendix*, Fig. S2). Theoretical calculations of the attractive interaction potential arising from depletion effects based on [77,78] are consistent with the shown experimental trends. Following the approach of [79], the potentials allow for an approximate estimation of the lifetimes of protein complexes stabilized via IRO, by considering the characteristic escape time of two particles from a potential well. The lifetime τ_l, adapted from Kramer's theory, is approximated as:

$$\tau_l = \frac{\Delta^2}{D} \exp\left(\frac{-U}{k_b T}\right) \tag{4}$$

where $\Delta \sim 0.1\sigma$, with $\sigma = 11.8$ nm corresponding to the ferritin diameter [80], D is the diffusion coefficient, and U denotes the potential depth in units $k_b T$. The resulting estimates based on our potential parameters are depicted in Fig. 3F. Higher dextran molecular weights lead to stronger depletion attraction and thus longer complex lifetimes. We note that the lifetimes are consistent with the relaxation times measured via MHz-XPCS. In particular for dextran500 at low q, the correlation functions do not fully decay within the available time window, indicating rather slow fluctuations of the IRO.

This observation may have significant implications for biological systems. While macromolecular crowding is generally known to reduce association rate constants by slowing diffusion, this effect can be counterbalanced by increased intermolecular attraction — such as that arising from depletion interactions — which can enhance binding rates [81–83]. The pronounced increase in attractive interactions observed under crowded conditions in our system could thus have a strong impact on protein–protein association dynamics including enzymatic catalysis and immune signaling via cytokines [84]. Since both the strength of attraction and the associated complex lifetimes scale with crowder molecular weight and concentration, these findings may help explain the variable, and at times contradictory effects of crowding reported in the literature [85, 86].

Self-diffusion is closely linked to variations of micro- and macroscopic viscosity arising from depletion effects. To investigate the impact of the standard crowders on single-protein diffusion, the microscopic self-diffusion coefficient is derived from the hydrodynamic function $H(q)$ in the high-q region, where $H(q \to \infty) = \frac{D_S^H}{D_0}$. Both $H(q \to \infty)$ and D_0 were obtained by modelling the measured $D(q)$. The concentration dependence of D_S^H is shown in Fig. 4A, revealing a largely molecular weight-independent behavior.

The macroscopic diffusion coefficient D_{SE} was calculated using the Stokes–Einstein equation, based on the measured macroscopic viscosities of the crowder solutions and the hydrodynamic radius of the ferritin ($R_h = 6.85$ nm [87]). Unlike D_S^H, D_{SE} shows a pronounced dependence on crowder molecular weight (Fig. 4B), suggesting that in dense solutions, local polymer structure—rather than total chain length—dominates in regulating protein mobility.

To further explore the discrepancy between D_S^H and D_{SE}, their ratio was plotted as a function of normalized crowder concentration c/c^* (Fig. 4C). The results show that D_S^H/D_{SE} does not scale with bulk viscosity and exhibits a non-monotonic concentration dependence. Notably, at high crowder concentrations, D_S^H can be up to eight times faster than predicted by D_{SE}, highlighting a clear decoupling between microscopic and macroscopic transport in crowded environments.

In order to understand the origin of this behavior, key parameters relevant to colloid–polymer solutions were determined. The dominant structural length scale in the semi-dilute regime, the correlation length ξ, was extracted by fitting SAXS curves of pure crowder solutions using an Ornstein-Zernike-like function [88–90]:

$$I(q) = \frac{I(0)}{1 + (q\,\xi)^b}, \tag{5}$$

where $\xi(c)$ and b are fitting parameters. The extracted correlation lengths, along with exponential functions as guides to the eyes, are shown in Fig. 4D. The inset provides example fits of SAXS curves for dextran100 using Eq.5. Using the correlation length ξ, the depletion layer thickness δ_s was estimated via [82] [91–93]

$$\delta_s = R\left(1 + 3\frac{\delta}{R} + 2.273\left(\frac{\delta}{R}\right)^2 - 0.0975\left(\frac{\delta}{R}\right)^3\right)^{1/3} - R, \tag{6}$$

with $\delta^{-2} = \delta_0^{-2} + \xi^{-2}$. δ_0 is the depletion layer thickness in dilute solutions, approximated by the polymer's radius of gyration R_g (see *SI Appendix*, Table S1). R corresponds to the radius of gyration of ferritin. The resulting δ_s values as a function of normalized crowder concentration ($c_{crowder}/c^*$) are shown in Fig. 4E. This allows to estimate the microscopic viscosity using the model proposed in [94]

$$\eta_{micro} = \eta_s \frac{Q(\lambda, \epsilon)}{Z(\lambda, \epsilon)}, \tag{7}$$

with the expressions for $Q(\lambda, \epsilon)$ and $Z(\lambda, \epsilon)$ provided in the *SI Appendix*. η_s is the solvent viscosity and η_{macro} the measured macroscopic viscosity. The parameters are defined as $\epsilon = \delta_s/R$ and $\lambda = \eta_s/\eta_{macro}$. The resulting concentration-dependent ratio $\eta_{macro}/\eta_{micro}$ is shown in Fig. 4F, mirroring the trend observed for the self-diffusion constant ratio D_S^H/D_{SE}.

This analysis suggests that the observed non-monotonic behavior originates from an interplay of microscopic and macroscopic viscosities, mediated by depletion effects. Within the depletion layer - where macromolecules are excluded - the microviscosity is significantly reduced. At low concentrations, the large depletion layer surrounding the protein allows thus for faster self-diffusion. As crowder concentration increases, the correlation length ξ decreases causing the depletion layer to shrink accordingly (see Fig. 4D & E), thereby restricting protein motion and leading to a sharper drop in D_S^H as it becomes more influenced by the rising bulk viscosity.

Beyond approximately $\sim 2c^*$, the depletion layer thickness stabilizes, while the macroscopic viscosity continues to increase steeply. This results in a more rapid decline of D_{SE} reversing the earlier trend. This crossover near $2c^*$ was observed for all polysaccharide crowders tested suggesting a universal behavior among these systems.

We also note that the absolute values in Fig. 4F differ by a factor of two or more from the experimental values in Fig. 4C, indicating that additional effects beyond the depletion layer must be contributing. In this context, the enhanced diffusion of nanoparticles in solutions with macromolecular crowders is well documented and has been attributed to the fact that nanoparticles experience the local polymer structure rather than the bulk properties of the

solution [46]. We therefore hypothesize that our experiments capture a combination of this known enhancement effect and the influence of the nanoscopic depletion layer leading to the non-monotonic behavior. We attribute these observations to the high sensitivity of XPCS to molecular-scale dynamics, which enables us to resolve the influence of structural features such as the depletion layer that may be less accessible using conventional optical methods.

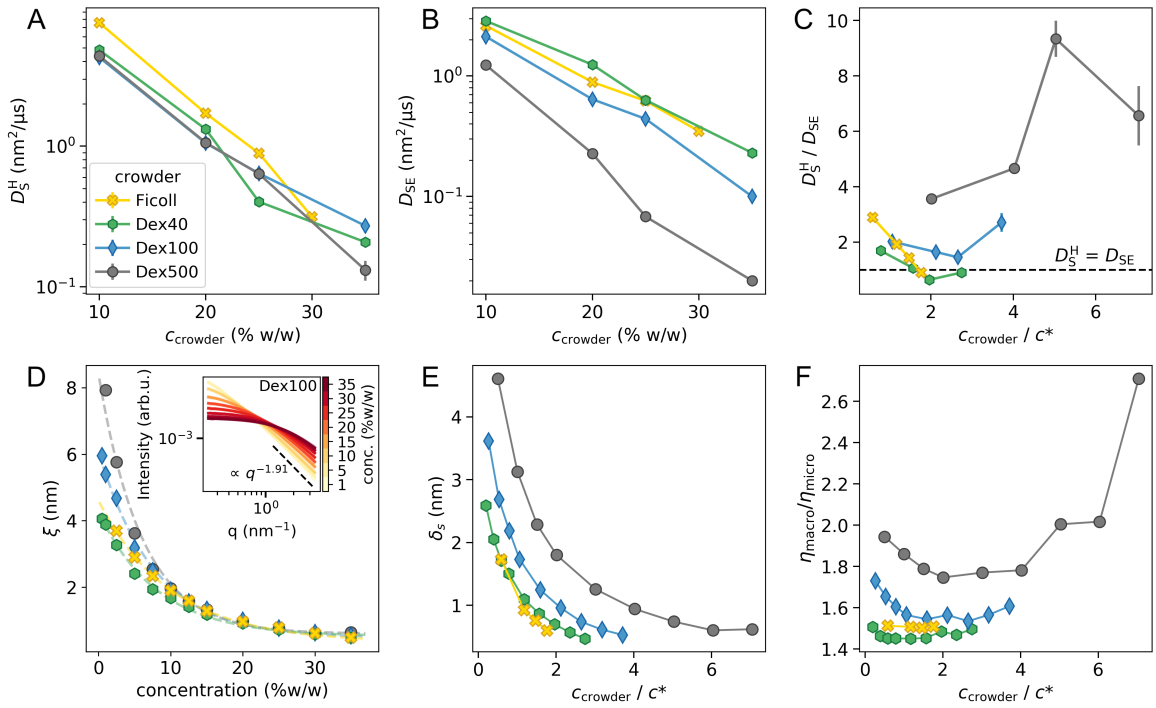

Fig. 4. Polysaccharide concentration and depletion effects on self-diffusion of ferritin. (A) Self-diffusion constant of ferritin on the microscopic scale (D_S^H) as a function of polysaccharide concentration. Error bars result from error propagation of D_0, determined via $D(q)$ fits. (B) Macroscopic self-diffusion constant (D_{SE}) as a function of polysaccharide concentration, calculated using Stokes-Einstein equation based on measured macroscopic viscosities of polysaccharide solutions. Error bars correspond to the error propagation based on uncertainty of the measured viscosities. (C) Ratio of microscopic to macroscopic self-diffusion constants as a function of crowder concentration normalized by the overlap concentration c^*. Error bars result from error propagation of D_S^H and D_{SE}. (D) Correlation length (ξ) of crowder solutions as a function of crowder concentration with dashed lines representing exponential functions as visual guides. ξ is obtained by fitting SAXS intensities of pure crowder solutions with an Ornstein-Zernike-like equation 5. Examplary fits for dextran100 are shown in the inset. (E) Theoretical depletion layer thickness δ_s, calculated based on ξ and R_g using Equation 6, depending on crowder concentration normalized by c^*. (F) Ratio of macro- to microviscosity of the crowder solution as a function of normalized crowder concentration ($c_{crowder}/c^*$). Microscopic viscosity values are theoretical and derived from η_s, η_{bulk} and δ_s using Equation 12.

Discussion

This study demonstrates that different types of crowder molecules induce distinct effects on protein dynamics. The collective dynamics of ferritin show that sucrose primarily maintains repulsive protein–protein interactions, whereas polysaccharide crowders introduce additional short-range attractions due to depletion interactions, a well-established phenomenon in colloid–polymer mixtures. These attractions lead to the formation of intermediate-range order (IRO) in ferritin–polysaccharide solutions, a universal effect observed for both dextran and Fi-

coll.

Despite their distinct conformations in solution — Ficoll forming compact, highly branched coils and dextran adopting more flexible, extended structures — short-range attraction consistently emerged once the polysaccharide overlap concentration was exceeded, highlighting the critical role of polymer concentration. Furthermore, increasing the molecular weight of dextran enhanced these attractions, resulting in more stable and longer-lived ferritin complexes via IRO. This underscores that even variations in molecular weight within the same crowder type can significantly modulate crowding effects.

Self-diffusion measurements on both macroscopic and microscopic scales revealed pronounced differences, with the ratio of microscopic to macroscopic diffusion coefficients displaying a non-monotonic dependence on crowder concentration. This behavior reflects the interplay between local depletion effects and bulk viscosity. Initially, the reduction in self-diffusion is attributed to the shrinking of the depletion layer; beyond the semi-dilute regime, however, the sharp increase in macroscopic viscosity dominates. Notably, normalizing by the overlap concentration c^* produced a universal scaling behavior, with a turning point around $2c^*$, beyond which macroscopic viscosity overrides depletion-induced mobility enhancements.

Our investigation of both collective and self-diffusion of ferritin under crowded conditions shows that: i) the interplay between proteins and crowders — including depletion interactions, ii) the type of crowder (e.g., hard-sphere-like vs. polymer-like) and its concentration-dependent structure, and iii) the crowder's molecular weight — all strongly influence nanoscale protein dynamics. These findings help explain the sometimes contradictory results reported in the literature regarding protein behavior under crowded conditions, such as in enzymatic reactions or protein association.

Ultimately, this work highlights the necessity of integrating polymer physics and depletion theory — alongside excluded volume effects — into models of crowded environments, especially when using polymeric crowders. Even so-called "standard" crowders can lead to nontrivial and system-specific behaviors, underscoring that crowding is not a one-size-fits-all phenomenon.

Materials and Methods

Sample preparation

Ferritin was purchased from Sigma Aldrich and corresponds to ferritin from equine spleen in saline solution (CAS: 9007-73-2) with an initial protein concentration of c= 71 mg/ml. To increase the protein concentration, 8 ml of this solution was centrifuged at 5000 g and 1.5 ml at 10000 g for 15 minutes using 30 kDa Millipore filters. Using SAXS calibration curves of ferritin solutions of known concentration, the resulting ferritin concentration was determined to be 110 mg/ml and 265 mg/ml.

Stock solutions of dextran40, dextran100 and dextran500 (Roth, CAS: 9004-54-0) were prepared in concentrations of 20, 40, 43.75 and 50 %w/w as well as of Ficoll®400 (Sigma Aldrich, CAS: 26873-85-8) and sucrose (Sigma Aldrich, CAS: 57-50-1) in concentrations of 20, 40, 50 and 60 %w/w by dissolving them in 103 mM saline solution with a pH value of 7.

To obtain a final dextran concentration of 35 %w/w in the sample, the 265 mg/ml ferritin solution was mixed with the 43.75 %w/w dextran stock in a 20% : 80% volume ratio. All the

other stock solutions were mixed 50% : 50% with the 110 mg/ml ferritin solution. The resulting crowder concentrations in the sample are therefore 10, 20, 25 and 35 %w/w using dextran as a crowder and 10, 20, 25 and 30 %w/w using surcrose and Ficoll as crowder. The ferritin concentration remains constant at approx. 55 mg/ml. The solutions were filled into quartz capillaries with an outer diameter of 1.5 mm and a wall thickness of 20 µm.

Experimental setup

Two experiments were carried out at the Material Imaging and Dynamics (MID) instrument of European XFEL to collect the data presented. In both cases the small-angle X-ray scattering (SAXS) configuration was used. The first experiment was performed using the pink beam with a photon energy of 9 keV. 200 pulses per train were delivered with a repetition rate of 2.2 MHz, which corresponds to a pulse spacing of 455 ns. For the second experiment the pink beam with a photon energy of 10 keV and a higher repetition rate of 4.5 MHz (222 ns pulse spacing) was available. The inter-train repetition rate was 10 Hz in both experiments. Using compound refractive lenses (CRL), the beam was focused to 14.5 µm and 14.2 µm in diameter. Using a scanning speed of 0.4 mm/s of the Fast-Solid-Sample Scanner ensures the refreshment of the sample volume in between the trains, as described in [47]. The data acquisition was realized by using the Adaptive Gain Integrating Pixel Detector (AGIPD) [95, 96], which was positioned 7.15 m and 7.687 m behind the sample. With this an available q-range of 0.1 to 1 nm^{-1} and 0.075 to 1 nm^{-1} was gained. All measurements were performed at room temperature (25°C).

XPCS calculations

The scattering of coherent X-rays by the ferritin particles within the sample system generates a speckle pattern that varies over time as a result of particle motion. To analyze the dynamics of the ferritin, the fluctuating intensities measured experimentally at two distinct times, t_1 and t_2, can be correlated. This approach employs two-time correlation functions of the form [64, 97, 98]:

$$C(q, t_1, t_2) = \frac{\langle I(q, t_1) I(q, t_2) \rangle_{\mathrm{pix}}}{\langle I(q, t_1) \rangle_{\mathrm{pix}} \langle I(q, t_2) \rangle_{\mathrm{pix}}} \tag{8}$$

where $\langle ... \rangle_{\mathrm{pix}}$ indicate the average of all detector pixels within the same q-range. In the first experiment, the q-binning was set to $\Delta q = 0.045$ nm, in the second to $\Delta q = 0.04$ nm. For a sufficient signal to noise ratio data was collected and averaged over several thousand trains. The intensity autocorrelation function, $g_2(q,t) = \langle C(q, t_1, t_1 + t) \rangle_{t_1}$, can be extracted by performing horizontal cuts along the t_1 axis, starting from the diagonal [99]. Based on the standard deviation of the fluctuating contrast values of the TTC, a weighted average over trains and times is calculated to determine the final $g_2(q,t)$ function. The error bars correspond to the square root of the inverse of the summed weights.

Modelling of S(q) and H(q)

The static structure factor $S(q)$ is calculated based on interparticle potentials present within the solution solving the Ornstein-Zernike equation with the mean spherical approximation closure. This is achieved with Python-based codes provided by the program *jscatter* [100]. Systems

containing short-range attraction and long-range repulsion can be described by a two-Yukawa potential as shown in Eq. 3 [71]. While the parameters regarding the repulsive part of the potential were kept constant, the parameters describing the attractive part, K_1 and scl_1, were adjusted during fitting. To describe systems with a mainly repulsive particle-particle interaction potential, a single-Yukawa potential was used. For this purpose the attractive potential strength parameter K_1 was set to 0, while K_2 and scl_2 were adjusted. In both cases, the protein radius and concentration are treated as constant parameters, with the radius of gyration of 5.9 nm [80] and the ferritin concentration set to 0.15 mmol/l.
The hydrodynamic function $H(q)$ was calculated applying the $\delta\gamma$ expansion from Beenakker and Mazur [72, 73]. This approach accounts for many body hydrodynamic interactions of spherical particles in suspension using the structure factor $S(q)$ as only input. As described in [101] the $H(q)$ was calculated using *jscatter* in accordance to the following expressions:

$$H(q) = H_d(q) + \frac{D_s(\Phi)}{D_0} \tag{9}$$

with

$$H_d(q) = \frac{3}{2\pi}\int_0^\infty dR_p k \frac{sin^2(R_p k)}{(R_p k)^2(1+\Phi S_\gamma(R_p k)}\int_{-1}^{1} dx(1-x^2)S(|q-k|-1) \tag{10}$$

$$\frac{D_s(\Phi)}{D_0} = \frac{2}{\pi}\int_0^\infty sinc^2(x)(1+\Phi S_\gamma(x))^{-1} \tag{11}$$

where $x = cos(q,k)$ represents the angle between the vectors q and k, Φ and R_p correspond to the protein volume fraction and the protein radius and $S_\gamma(x)$ is given by [101].

Acknowledgements

We acknowledge European XFEL in Schenefeld, Germany, for providing X-ray free-electron laser beamtime at Materials Imgaging and Dynamics (MID) instrument and would like to thank the staff for their support. The data presented here were collected during two beamtimes allocated to proposals 3348 and 5397. This work was supported by the Maxwell computational resources of the Deutsches Elektronen-Synchrotron DESY, Hamburg, Germany. Furthermore, we acknowledge DELTA machine group for providing synchrotron radiation and for technical support. We thank Marvin Kowalski, Jenny Schrage, Pia Kwiasowski, Maximilian Senft, Prince Prabhu Rajaiah, Lara Reichart, and Chang Hee Woo for their collaboration during beamtime and Randeer Gautam for the discussion of the experimental results.

Funding: We acknowledge BMBF (05K19PS1, 05K20PSA and 05K22PS1)(to C.G.); 05K19VTB, (to F.S. and F.Z.), DFG-ANR (SCHR700/28-1, SCHR700/42-1, ANR-16-CE92-0009) (to F.S. and F.Z.). We acknowledge funding from NFDI 40/1 (DAPHNE4NFDI). F.P., I.A.A., and A.G. acknowledge funding from the European Union's Horizon Europe research and innovation programme under the Marie Skłodowska-Curie grant agreement No. 101081419 (PRISMAS) (F.P. and I.A.A.) and 101149230 (CRYSTAL-X) (F.P. and A.G.). F.P. acknowledges financial support by the Swedish National Research Council (Vetenskapsrådet) under Grant No. 2019-05542, 2023-05339 and within the Röntgen-Ångström Cluster Grant No. 2019-06075, and the kind

financial support from Knut och Alice Wallenberg foundation (WAF, Grant. No. 2023.0052). This research is supported by the Center of Molecular Water Science (CMWS) of DESY in an Early Science Project, the MaxWater initiative of the Max-Planck-Gesellschaft (Project No. CTS21:1589), Carl Tryggers and the Wenner-Gren Foundations (Project No. UPD2021-0144).

Author contributions

M.D., N.D.A, M.P. and C.G. designed the experiments, along with discussions with F.S., F.P., F.Z, and F.L.. M.D., N.D.A., A.G., M.B., and J.S. prepared the samples. M.D., N.D.A., A.G., S.R., S.T., A.M.R., A.L., F.U., I.A., M.B., C.H.W., P.K., L.R., F.L., M.P., and C.G. conducted the experiment. J.M., W.J., F.B., U.B., J.H., J.P., A.R., R.S., M.Y., A.Z., and A.M. operated MID instrument. J.M., F.B., and A.L., provided the data analysis pipeline. M.D. performed the data processing and analysis. M.D., N.D.A., M.P., C.G., F.Z., and F.S. discussed the XPCS data analysis with input from S.R., A.G., F.P., J.M., and F.L.. The manuscript was written by M.D., M.P., and C.G. with input from all authors.

Competing interests The authors declare no competing interest.

Data availability Data recorded at the European XFEL are available at DOI: 10.22003/XFEL.EU-DATA-003348-00 and DOI:10.22003/XFEL.EU-DATA-005397-00. The data collected at DELTA and the code used to analyze the data is available from the corresponding authors upon request.

References

[1] Ellis RJ (2001) Macromolecular crowding: obvious but underappreciated. *Trends Biochem. Sci.* 26(10):597–604.

[2] Yu I, et al. (2016) Biomolecular interactions modulate macromolecular structure and dynamics in atomistic model of a bacterial cytoplasm. *elife* 5:e19274.

[3] Roosen-Runge F, et al. (2011) Protein self-diffusion in crowded solutions. *Proc. Natl. Acad. Sci. U. S. A.* 108(29):11815–11820.

[4] Luby-Phelps K (1999) Cytoarchitecture and physical properties of cytoplasm: volume, viscosity, diffusion, intracellular surface area. *Int. Rev. Cytol.* 192:189–221.

[5] Heinen M, et al. (2012) Viscosity and diffusion: crowding and salt effects in protein solutions. *Soft Matter* 8(5):1404–1419.

[6] Dix JA, Verkman A (2008) Crowding effects on diffusion in solutions and cells. *Annu. Rev. Biophys.* 37(1):247–263.

[7] Gnutt D, Ebbinghaus S (2016) The macromolecular crowding effect–from in vitro into the cell. *Biol. Chem.* 397(1):37–44.

[8] Laurent TC, Ogston A (1963) The interaction between polysaccharides and other macromolecules. 4. the osmotic pressure of mixtures of serum albumin and hyaluronic acid. *Biochemical Journal* 89(2):249.

[9] Minton AP (1981) Excluded volume as a determinant of macromolecular structure and reactivity. *Biopolymers* 20(10):2093–2120.

[10] Minton A, Wilf J (1981) Effect of macromolecular crowding upon the structure and function of an enzyme: glyceraldehyde-3-phosphate dehydrogenase. *Biochemistry* 20(17):4821–4826.

[11] Minton AP (1997) Influence of excluded volume upon macromolecular structure and associations in "crowded" media. *Curr. Opin. Biotechnol.* 8(1):65–69.

[12] Minton AP (2001) The influence of macromolecular crowding and macromolecular confinement on biochemical reactions in physiological media. *J. Biol. Chem.* 276(14):10577–10580.

[13] Ranganathan VT, Bazmi S, Wallin S, Liu Y, Yethiraj A (2022) Is ficoll a colloid or polymer? a multitechnique study of a prototypical excluded-volume macromolecular crowder. *Macromolecules* 55(20):9103–9112.

[14] Biswas S, Kundu J, Mukherjee SK, Chowdhury PK (2018) Mixed macromolecular crowding: a protein and solvent perspective. *ACS omega* 3(4):4316–4330.

[15] Rusinga FI, Weis DD (2017) Soft interactions and volume exclusion by polymeric crowders can stabilize or destabilize transient structure in disordered proteins depending on polymer concentration. *Proteins: Struct., Funct., Bioinf.* 85(8):1468–1479.

[16] Mardoum WM, Gorczyca SM, Regan KE, Wu TC, Robertson-Anderson RM (2018) Crowding induces entropically-driven changes to dna dynamics that depend on crowder structure and ionic conditions. *Front. Phys.* 6:53.

[17] Colby RH (2010) Structure and linear viscoelasticity of flexible polymer solutions: comparison of polyelectrolyte and neutral polymer solutions. *Rheol. acta* 49:425–442.

[18] Teraoka I (2002) *Polymer solutions.* (Wiley).

[19] Hirata Y, et al. (2003) Small-angle x-ray scattering studies of moderately concentrated dextran solution. *Carbohydr. Polym.* 53(3):331–335.

[20] Asakura S, Oosawa Fm (1954) On interaction between two bodies immersed in a solution of macromolecules. *J. Chem. Phys.* 22(7):1255–1256.

[21] Vrij A (1976) Polymers at interfaces and the interactions in colloidal dispersions. *Pure Appl. Chem.* 48(4):471–483.

[22] Tuinier R, Lekkerkerker HN (2011) *Colloids and the depletion interaction.* (Springer Netherlands).

[23] Neu B, Meiselman HJ (2006) Depletion interactions in polymer solutions promote red blood cell adhesion to albumin-coated surfaces. *Biochim. Biophys. Acta - Gen. Subj.* 1760(12):1772–1779.

[24] Rampling M, Meiselman H, Neu B, Baskurt O (2004) Influence of cell-specific factors on red blood cell aggregation. *Biorheology* 41(2):91–112.

[25] Smith NJ, Williams PA (1995) Depletion flocculation of polystyrene latices by water-soluble polymers. *J. Chem. Soc. Faraday Trans.* 91(10):1483–1489.

[26] Zhang H, Kong D, Zhang W, Liu H (2023) Depletion attraction in colloidal and bacterial systems. *Front. Mater.* 10:1206819.

[27] Gögelein C, Nägele G, Buitenhuis J, Tuinier R, Dhont JK (2009) Polymer depletion-driven cluster aggregation and initial phase separation in charged nanosized colloids. *J. Chem. Phys.* 130(20).

[28] Fries J, et al. (2025) Chemically active droplets in crowded environments. *arXiv preprint arXiv:2505.11188.*

[29] Tuinier R, Dhont J, De Kruif C (2000) Depletion-induced phase separation of aggregated whey protein colloids by an exocellular polysaccharide. *Langmuir* 16(4):1497–1507.

[30] Banani SF, Lee HO, Hyman AA, Rosen MK (2017) Biomolecular condensates: organizers of cellular biochemistry. *Nat. Rev. Mol. Cell Biol.* 18(5):285–298.

[31] von Bülow S, Siggel M, Linke M, Hummer G (2019) Dynamic cluster formation determines viscosity and diffusion in dense protein solutions. *Proceedings of the National Academy of Sciences* 116(20):9843–9852.

[32] Liu Y, et al. (2011) Lysozyme protein solution with an intermediate range order structure. *J. Phys. Chem. B* 115(22):7238–7247.

[33] Alfano C, et al. (2024) Molecular crowding: the history and development of a scientific paradigm. *Chem. Rev.* 124(6):3186–3219.

[34] Höfling F, Franosch T (2013) Anomalous transport in the crowded world of biological cells. *Rep. Prog. Phys.* 76(4):046602.

[35] Metzler R, Jeon JH, Cherstvy AG, Barkai E (2014) Anomalous diffusion models and their properties: non-stationarity, non-ergodicity, and ageing at the centenary of single particle tracking. *Phys. Chem. Chem. Phys.* 16(44):24128–24164.

[36] Szymanski J, Weiss M (2009) Elucidating the origin of anomalous diffusion in crowded fluids. *Phys. Rev. Lett.* 103(3):038102.

[37] Lampo TJ, Stylianidou S, Backlund MP, Wiggins PA, Spakowitz AJ (2018) Cytoplasmic rna-protein particles exhibit non-gaussian subdiffusive behavior. *Biophys. J.* 112(3):532–542.

[38] Sabri A, Xu X, Krapf D, Weiss M (2020) Elucidating the origin of heterogeneous anomalous diffusion in the cytoplasm of mammalian cells. *Phys. Rev. Lett.* 125(5):058101.

[39] Homchaudhuri L, Sarma N, Swaminathan R (2006) Effect of crowding by dextrans and ficolls on the rate of alkaline phosphatase–catalyzed hydrolysis: A size-dependent investigation. *Biopolymers* 83(5):477–486.

[40] Derham BK, Harding JJ (2006) The effect of the presence of globular proteins and elongated polymers on enzyme activity. *Biochim. Biophys. Acta - Proteins Proteom.* 1764(6):1000–1006.

[41] Ren G, Lin Z, Tsou Cl, Wang Cc (2003) Effects of macromolecular crowding on the unfolding and the refolding of d-glyceraldehyde-3-phosophospate dehydrogenase. *J. Protein Chem.* 22:431–439.

[42] Wenner JR, Bloomfield VA (1999) Crowding effects on ecorv kinetics and binding. *Biophys. J.* 77(6):3234–3241.

[43] Pastor I, et al. (2011) Effect of crowding by dextrans on the hydrolysis of n-succinyl-l-phenyl-ala-p-nitroanilide catalyzed by α-chymotrypsin. *J. Phys. Chem. B* 115(5):1115–1121.

[44] Norris MG, Malys N (2011) What is the true enzyme kinetics in the biological system? an investigation of macromolecular crowding effect upon enzyme kinetics of glucose-6-phosphate dehydrogenase. *Biochem. Biophys. Res. Commun.* 405(3):388–392.

[45] Okamoto DN, et al. (2010) Increase of sars-cov 3cl peptidase activity due to macromolecular crowding effects in the milieu composition. *Biol. Chem.* 391:1461–1468.

[46] Kohli I, Mukhopadhyay A (2012) Diffusion of nanoparticles in semidilute polymer solutions: effect of different length scales. *Macromolecules* 45(15):6143–6149.

[47] Reiser M, et al. (2022) Resolving molecular diffusion and aggregation of antibody proteins with megahertz x-ray free-electron laser pulses. *Nat. Commun.* 13(5528).

[48] Girelli A, et al. (2024) Coherent x-rays reveal anomalous molecular diffusion and cage effects in crowded protein solutions. *arXiv preprint arXiv:410.08873*.

[49] Theil EC (1990) *The Ferritin Family of Iron Storage Proteins*. (John Wiley & Sons, Ltd), pp. 421–449.

[50] Harrison PM, Arosio P (1996) The ferritins: molecular properties, iron storage function and cellular regulation. *Biochim. Biophys. Acta - Bioenerg.* 1275(3):161–203.

[51] Chasteen ND, Harrison PM (1999) The ferritins: molecular properties, iron storage function and cellular regulation. *J. Struct. Biol.* 126:182–194.

[52] Rodrigues MQ, Alves PM, Roldão A (2021) Functionalizing ferritin nanoparticles for vaccine development. *Pharmaceutics* 13(1621).

[53] Khoshnejad M, Parhiz H, Shuvaev VV, Dmochowski IJ, Muzykantov VR (2018) Ferritin-based drug delivery systems: Hybrid nanocarriers for vascular immunotargeting. *J. Control. Release* 282:13–24.

[54] Lucignano R, et al. (2024) Human ferritin nanocarriers for drug-delivery: A molecular view of the disassembly process. *Int. J. Biol. Macromol.* 277(2).

[55] Madsen A, et al. (2021) Materials imaging and dynamics (mid) instrument at the european x-ray free-electron laser facility. *J. Synchrotron Radiat.* 28(2):637–649.

[56] Dargasz M, et al. (2022) X-ray scattering at beamline bl2 of delta: Studies of lysozyme-lysozyme interaction in heavy water and structure formation in 1-hexanol in *J. Phys.: Conf. Ser.* (IOP Publishing), Vol. 2380, p. 012031.

[57] Williams G, Watts DCN (1970) Non-symmetrical dielectric relaxation behaviour arising from a simple empirical decay function. *Trans. Faraday Soc.* 66(80).

[58] Hruszkewycz S, et al. (2012) High contrast x-ray speckle from atomic-scale order in liquids and glasses. *Phys. Rev. Lett.* 109,:185502.

[59] Lehmkühler F, et al. (2020) Emergence of anomalous dynamics in soft matter probed at the european xfel. *Proc. Natl. Acad. Sci. U.S.A.* 117,:24110–24116.

[60] Omari RA, Aneese AM, Grabowski CA, Mukhopadhyay A (2009) Diffusion of nanoparticles in semidilute and entangled polymer solutions. *J. Phys. Chem. B* 113(25):8449–8452.

[61] Banks DS, Fradin C (2005) Anomalous diffusion of proteins due to molecular crowding. *Biophys. J.* 89(5):2960–2971.

[62] Sanabria H, Kubota Y, Waxham MN (2007) Multiple diffusion mechanisms due to nanostructuring in crowded environments. *Biophys. J.* 92(1):313–322.

[63] de Val N, Declercq JP, Limc CK, Crichton RR (2012) Structural analysis of haemin demetallation by l-chain apoferritins. *J. Inorg. Biochem.* 112:77–84.

[64] Lehmkühler F, Roseker W, Grübel G (2021) From femtoseconds to hours-measuring dynamics over 18 orders of magnitude with coherent x-rays. *Appl. Sci.* 11(6179).

[65] Nägele G (1996) On the dynamics and structure of charge-stabilized suspensions. *Phys. Rep.* 272(5-6):215–372.

[66] Pusey P (1975) The dynamics of interacting brownian particles. *J. Phys. A: Math. Gen.* 8(9):1433.

[67] Zhang F, et al. (2024) Effective interactions in protein solutions with and without clustering. *Phys. A: Stat. Mech. Appl.* 650:129995.

[68] Porcar L, et al. (2010) Formation of the dynamic clusters in concentrated lysozyme protein solutions. *J. Phys. Chem. Lett.* 1(1):126–129.

[69] Liu Y, et al. (2011) Lysozyme protein solution with an intermediate range order structure. *J. Phys. Chem. B* 115(22):7238–7247.

[70] Yearley EJ, et al. (2014) Observation of small cluster formation in concentrated monoclonal antibody solutions and its implications to solution viscosity. *Biophys. J.* 106,:1763–1770.

[71] Liu Y, Chen WR, Chen SH (2005) Cluster formation in two-yukawa fluids. *J. Chem. Phys.* 122(4).

[72] Beenakker C, Mazur P (1984) Diffusion of spheres in a concentrated suspension ii. *Phys. A Stat. Mech. Its Appl.* 126,:349–370.

[73] Beenakker C, Mazur P (1983) Self-diffusion of spheres in a concentrated suspension. *Phys. A Stat. Mech. Its Appl.* 120,:388–410.

[74] Riest J, Nägele G (2015) Short-time dynamics in dispersions with competing short-range attraction and long-range repulsion. *Soft Matter* 11(48):9273–9280.

[75] Li J, Busscher HJ, Norde W, Sjollema J (2011) Analysis of the contribution of sedimentation to bacterial mass transport in a parallel plate flow chamber. *Colloids Surf. B: Biointerfaces* 84(1):76–81.

[76] Hinderliter PM, et al. (2010) Isdd: A computational model of particle sedimentation, diffusion and target cell dosimetry for in vitro toxicity studies. *Part. Fibre Toxicol.* 7:1–20.

[77] Ilett SM, Orrock A, Poon W, Pusey P (1995) Phase behavior of a model colloid-polymer mixture. *Phys. Rev. E* 51(2):1344.

[78] Chatterjee AP, Schweizer KS (1998) Microscopic theory of polymer-mediated interactions between spherical particles. *J. Chem. Phys.* 109(23):10464–10476.

[79] Cardinaux F, et al. (2011) Cluster-driven dynamical arrest in concentrated lysozyme solutions. *J. Phys. Chem. B* 115(22):7227–7237.

[80] Wieland DCF, et al. (2021) Asaxs measurements on ferritin and apoferritin at the biosaxs beamline p12 (petra iii, desy). *J. Appl. Cryst.* 54:830–838.

[81] Berezhkovskii AM, Szabo A (2016) Theory of crowding effects on bimolecular reaction rates. *J. Phys. Chem. B* 120(26):5998–6002.

[82] Zosel F, Soranno A, Buholzer KJ, Nettels D, Schuler B (2020) Depletion interactions modulate the binding between disordered proteins in crowded environments. *Proc. Natl. Acad. Sci. U.S.A.* 117(24):13480–13489.

[83] Zhou HX, Rivas G, Minton AP (2008) Macromolecular crowding and confinement: biochemical, biophysical, and potential physiological consequences. *Annu. Rev. Biophys.* 37(1):375–397.

[84] Schreiber G, Haran G, Zhou HX (2009) Fundamental aspects of protein- protein association kinetics. *Chem. Rev.* 109(3):839–860.

[85] Kuznetsova IM, Turoverov KK, Uversky VN (2014) What macromolecular crowding can do to a protein. *Int. J. Mol. Sci.* 15(12):23090–23140.

[86] Mittal S, Chowhan RK, Singh LR (2015) Macromolecular crowding: Macromolecules friend or foe. *Biochim. Biophys. Acta - Gen. Subj.* 1850(9):1822–1831.

[87] Mohanty A, , et al. (2021) Kinetics of ferritin self-assembly by laser light scattering: Impact of subunit concentration, ph, and ionic strength. *Biomacromolecules* 22:1389–1398.

[88] Colby R (2010) Structure and linear viscoelasticity of flexible polymer solutions: comparison of polyelectrolyte and neutral polymer solutions. *Rheol. Acta* 49:425–442.

[89] Pedersen JS, Schurtenberger P (2004) Scattering functions of semidilute solutions of polymers in a good solvent. *J. Polym. Sci. B Polym. Phys.* 42(17):3081–3094.

[90] Higgins JS, Benoit HC (1994) Polymers and neutron scattering. *Oxf. Univ. Press.*

[91] Fleer GJ, Skvortsov AM, Tuinier R (2003) Mean-field equation for the depletion thickness. *Macromolecules* 36(20):7857–7872.

[92] Tuinier R, Lekkerkerker H, Aarts D (2002) Interaction potential between two spheres mediated by excluded volume polymers. *Phys. Rev. E* 65(6):060801.

[93] Hanke A, Eisenriegler E, Dietrich S (1999) Polymer depletion effects near mesoscopic particles. *Phys. Rev. E* 59(6):6853.

[94] Tuinier R, Dhont J, Fan TH (2006) How depletion affects sphere motion through solutions containing macromolecules. *Europhys. Lett.* 75(6):929.

[95] Allahgholi A, , et al. (2019) The adaptive gain integrating pixel detector at the european xfel. *J. Synchrotron Rad.* 26:74–82.

[96] Sztuk-Dambietz J, et al. (2024) Operational experience with adaptive gain integrating pixel detectors at european xfel. *Front. Phys.* 11.

[97] Perakis F, Gutt C (2020) Towards molecular movies with x-ray photon correlation spectroscopy. *Phys. Chem. Chem. Phys.* 22:19443–19453.

[98] Sutton M, Laaziri K, Livet F, Bley F (2003) Using coherence to measure two-time correlation functions. *Opt. Express* 11(19):2268–2277.

[99] Bikondoa O (2017) On the use of two-time correlation functions for x-ray photon correlation spectroscopy data analysis. *J. Appl. Crystallogr.* 50(2):357–368.

[100] Biehl R (2019) Jscatter, a program for evaluation and analysis of experimental data. *PLoS ONE* 14(6).

[101] Genz U, Klein R (1991) Collective diffusion of charged spheres in the presence of hydrodynamic interaction. *Phys. A Stat. Mech. Its Appl.* 171,:26–42.

[102] Granath KA (1958) Solution properties of branched dextrans. *J. Colloid Sci.* 13(4):308–328.

[103] Spencer SJ, Ranganathan VT, Yethiraj A, Andrews GT (2024) Concentration dependence of elastic and viscoelastic properties of aqueous solutions of ficoll and bovine serum albumin by brillouin light scattering spectroscopy. *Langmuir* 40(9):4615–4622.

Supporting Information:
Depletion-Induced Intermediate-Range Order Modulates Nanoscale Protein Diffusion in Polymeric Crowder Solutions

Michelle Dargasz [1*], Nimmi Das Anthuparambil[1], Sebastian Retzbach[2], Anita Girelli[3], Sonja Timmermann[1], Johannes Möller[4], Wonhyuk Jo[4], Aliaksandr Lenonau[1,4], Agha Mohammad Raza[1], Maddalena Bin[3], Jaqueline Savelkouls[5], Iason Andronis[3], Frederik Unger[1], Felix Brausse[4], Jörg Hallmann[4], Ulrike Boesenberg[4], Jan-Etienne Pudell[4], Angel Rodriguez-Fernandez[4], James Wrigley[4], Roman Shayduk[4], Mohamed Youssef[4], Alexey Zozulya[4], Anders Madsen[4], Felix Lehmkühler[6,7], Fivos Perakis[3], Fajun Zhang[2], Frank Schreiber[2], Michael Paulus[5], Christian Gutt [1†]

[1]Department Physik, Universität Siegen, Walter-Flex-Strasse 3, 57072 Siegen, Germany
[2]Institut für Angewandte Physik, Universität Tübingen, Auf der Morgenstelle 10, 72076 Tübingen, Germany
[3]Department of Physics, AlbaNova University Center, Stockholm University, 10691 Stockholm, Sweden
[4]European X-Ray Free-Electron Laser Facility, Holzkoppel 4,22869 Schenefeld, Germany
[5]Fakultät Physik/DELTA, TU Dortmund, 44221 Dortmund, Germany
[6]The Hamburg Centre for Ultrafast Imaging, Luruper Chaussee 149, 22761 Hamburg, Germany
[7]Deutsches Elektronen-Synchrotron DESY, Notkestr. 85, 22607 Hamburg, Germany

*Corresponding author. Email: michelle.dargasz@uni-siegen.de
†Corresponding author. Email: christian.gutt@uni-siegen.de

This PDF file includes:

Supplementary text
Figure S1 and S2
Table S1 and S2

Comparison of scattering intensities

Fig.S1 shows the comparison of the background subtracted small-angle X-ray scattering (SAXS) intensity profiles for pure ferritin (55 mg/ml), ferritin-crowder mixture, and the pure crowder solution, using dextran100 and sucrose as representative examples. The crowder concentration is 25 %w/w in all cases. The scattering intensities observed for the ferritin-crowder mixtures exceed that of the pure crowder solutions by more than two orders of magnitude, showing that the dominant contribution to the scattering in the mixtures arises from ferritin.

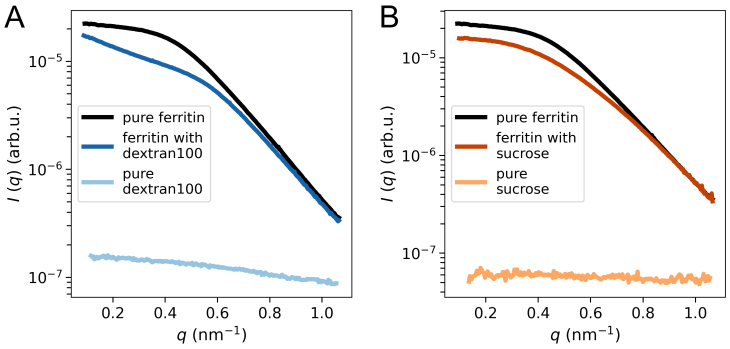

Fig. S1. Background subtracted small-angle X-ray scattering (SAXS) intensities for pure ferritin, ferritin-crowder and pure crowder solutions exemplarily for (A) dextran100 and (B) sucrose. The ferritin concentration is 55 mg/ml and the crowder concentration 25 %w/w in all cases.

Crowder-specific parameters

Table S1 summarizes the relevant parameters for the polymeric crowders used in this study. Listed are the molecular weights (M_w), the corresponding radii of gyration (R_g) as reported in [13, 102], and the overlap concentrations (c^*). For the dextrans, c^* was determined by macroscopic viscosity measurements using a rotational viscometer, while for Ficoll, the overlap concentration was adopted from [103].

crowder	M_w (g/mol)	R_g (nm)	c^* (%w/w)
Ficoll	400 000	11.07	17
dextran40	40 000	6.2	12.75
dextran100	100 000	9.5	9.42
dextran500	500 000	20	4.97

Table S1. Overview of the molecular weights (M_w), radii of gyration (R_g) and overlap concentrations (c^*) for the used polymeric crowder molecules dextran and Ficoll.

Interaction potentials derived from D(q) analysis

The single-Yukawa and two-Yukawa potentials $V(r)$ used for modeling the $D(q)$ of ferritin are displayed in Fig.S2 for all crowder solutions. The parameters used to compute these potentials are provided in Table S2. As the parameters of the single-Yukawa potential applied to sucrose solutions remain constant for all crowder concentrations and only D_0 is adjusted, the potential shown in Fig. S2(E) does not vary with concentration.

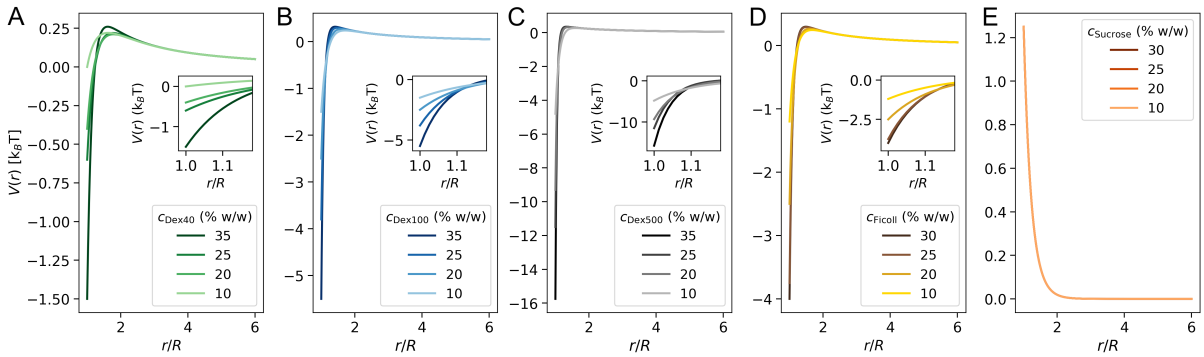

Fig. S2. Resulting two-Yukawa and single-Yukawa interaction potentials $V(r)$ of ferritin particles in solution with (A) dextran40, (B) dextran100, (C) dextran500, (D) Ficoll, and (E) sucrose. The insets highlight the varying potential depths.

crowder	conc. (%w/w)	K_1 (k_BT)	scl_1 (nm)	K_2 (k_BT)	scl_2 (nm)	D_0 (nm^2/µm)
sucrose	10			-1.25	1/3.5	19.7 ± 0.3
	20			-1.25	1/3.5	12 ± 0.2
	25			-1.25	1/3.5	8.9 ± 0.2
	30			-1.25	1/3.5	6 ± 0.15
Ficoll	10	1.7	1/5	-0.5	1/0.1	9 ± 0.3
	20	3	1/7	-0.5	1/0.1	2.065 ± 0.1
	25	4.25	1/9.5	-0.5	1/0.1	1.06 ± 0.03
	30	4.5	1/10	-0.5	1/0.1	0.38 ± 0.02
dextran40	10	0.5	1/2.4	-0.5	1/0.1	5.9 ± 0.2
	20	0.9	1/3	-0.5	1/0.1	1.57 ± 0.03
	25	1.1	1/3.5	-0.5	1/0.1	0.49 ± 0.02
	35	2	1/6	-0.5	1/0.1	0.255 ± 0.015
dextran100	10	2	1/5	-0.5	1/0.1	5.05 ± 0.3
	20	3	1/7.1	-0.5	1/0.1	1.24 ± 0.05
	25	4.3	1/10	-0.5	1/0.1	0.755 ± 0.025
	35	6	1/13	-0.5	1/0.1	0.32 ± 0.035
dextran500	10	5.3	1/8.2	-0.5	1/0.1	5.3 ± 0.15
	20	9.8	1/15	-0.5	1/0.1	1.275 ± 0.045
	25	12	1/19	-0.5	1/0.1	0.8 ± 0.05
	35	16.25	1/20.5	-0.5	1/0.1	0.16 ± 0.025

Table S2. Parameters used for modeling the $D(q)$ using a single-Yukawa and two-Yukawa interaction potential. K_1 accounts for the strength of the attractive part of the potential and K_2 for the repulsive part. The corresponding screening lengths are given by scl_i. D_0 refers to the diffusion constant at infinite dilution.

Estimation of the microscopic viscosity

The microscopic viscosity of crowder solutions was estimated based on the model of [94]:

$$\eta_{micro} = \eta_s \frac{Q(\lambda, \epsilon)}{Z(\lambda, \epsilon)} \tag{12}$$

with η_s indicating to the solvent viscosity. $Q(\lambda, \epsilon)$ and $Z(\lambda, \epsilon)$ are defined as:

$$
\begin{aligned}
Q(\lambda, \epsilon) &= 2(2+3\lambda)(1+\epsilon)^6 - 4(1-\lambda)(1+\epsilon) \\
Z(\lambda, \epsilon) &= 2(2+3\lambda)(1+\epsilon)^6 - 9\left(1 - \frac{1}{3}\lambda - \frac{2}{3}\lambda^2\right)(1+\epsilon)^5 \\
&\quad + 10(1-\lambda)(1+\epsilon)^3 - 9(1-\lambda)(1+\epsilon) + 4(1-\lambda)^2, \\
&\quad \text{with } \epsilon = \frac{\delta_s}{R} \text{ and } \lambda = \frac{\eta_s}{\eta_{macro}}
\end{aligned}
$$

Here, η_{macro} denotes the macroscopic bulk viscosity of the crowder solutions, δ_s represents the depletion layer thickness, and R corresponds to the radius of gyration of ferritin.